Nonlinear modeling of drop size distributions produced by pressure-swirl atomizers

Ki Sun Park, Stephen D. Heister *

School of Aeronautics and Astronautics, Purdue University, 701 W. Stadium Ave., W. Lafayette, IN 47907-2045, USA

ARTICLE INFO

ABSTRACT

An axisymmetric boundary element method (BEM) has been developed to simulate atomization processes in a pressure-swirl atomizer. Annular ligaments are pinched from the parent sheet and presumed to breakup via the linear stability model due to Ponstein. Corrections to Ponstein's result are used to predict satellite droplet sizes formed during this process. The implementation provides a first-principles capability to simulate drop size distributions for low viscosity fluids. Results show reasonable agreement with measured droplet size distributions and the predicted SMD is 30–40% smaller than experiment. The model predicts a large number of very small droplets that cannot typically be resolved in an experimental observation of the spray. A quasi-3-D spray visualization is presented by tracking droplets in a Lagrangian fashion from their formation point within the ring-shaped ligaments. A complete simulation is provided for a case generating over 80,000 drops.

1. Introduction

A pressure-swirl atomizer or simplex nozzle has been widely used in a number of industries. For example, this type of atomizer is commonly used in gas turbine applications for injecting fuel into the combustor and for a number of agricultural spraying processes. A simplex nozzle generally consists of three main parts; tangential inlet ports, a swirl chamber, and an exit orifice as indicated in Fig. 1. An exit orifice is preceded by a swirl chamber with a certain contraction angle. Several inlet ports are utilized to create the vortical flow within the swirl/vortex chamber and at sufficient inlet flow velocities an air core evolves naturally within the center of this chamber. Under normal operation, the air-core extends outside the orifice creating a thin annular cone-shaped flow. The linear theory for operation of the element is well established and a variety of models exist (Lefebvre, 1989; Bayvel and Orzechowski, 1993; Yule and Chinn, 1994; Bazarov and Yang, 1998) to provide a prediction of film thickness at the nozzle exit and the resultant cone angle for the spray as a function of injector design in inflow conditions.

Scaling arguments have been made in an attempt to correlate Sauter Mean Diameter (SMD) with these parameters and as a basis for empirically based models (Rizk and Lefebvre, 1985; Suyari and Lefebvre, 1986; Lefebvre, 1989). This process requires tedious measurements at a range of flow conditions and the resultant correlations are presumed to hold only for that particular injector/

atomizer geometry that was tested. More recently, stability analyses have been used to predict drop sizes by Cousin et al. (1996), Han et al. (1997) and Liao et al. (1999). Historical modeling of the spray may simply use a representative diameter (SMD) rather than a replication of the entire drop size distribution.

Higher level spray models have typically employed a variety of distribution functions (Rosin Rammler, Nukiyama–Tanasawa, etc.) to provide an analytic description of the spray that requires only a few inputs from experimental measurements. Unfortunately, simulations for many engineering problems display a high degree of sensitivity to the overall distribution within the spray thereby placing substantial requirements on the modeler to improve the distribution functions to the greatest extent possible. For example, in combustion problems, the ignition kinetics are dominated by the smallest drops while the overall combustion time/efficiency is chiefly determined by the largest drops, i.e., the tails of the distribution function are terribly important to the overall modeling result.

For these reasons, there is a strong motivation to develop spray distributions from first principles such that the vagaries of the fitting of the distribution function are no longer an issue. The ever-increasing computational power now affords modelers a limited capability to conduct such simulations and that serves as the motivation for the subject work.

The simplex nozzle is an ideal testbed for the development of analytic/computational spray distributions because these injectors produce a reasonably axisymmetric swirling sheet that serves as the initial condition for atomization events. For modest injection speeds, ligaments with significant azimuthal extent are observed to be pinched from the periphery of the conical sheet (Kim et al.,

---

* Corresponding author. Tel.: +1 765 494 5126; fax: +1 765 494 0307.
E-mail addresses: sunnypark@purdue.edu (K.S. Park), heister@purdue.edu (S.D. Heister).
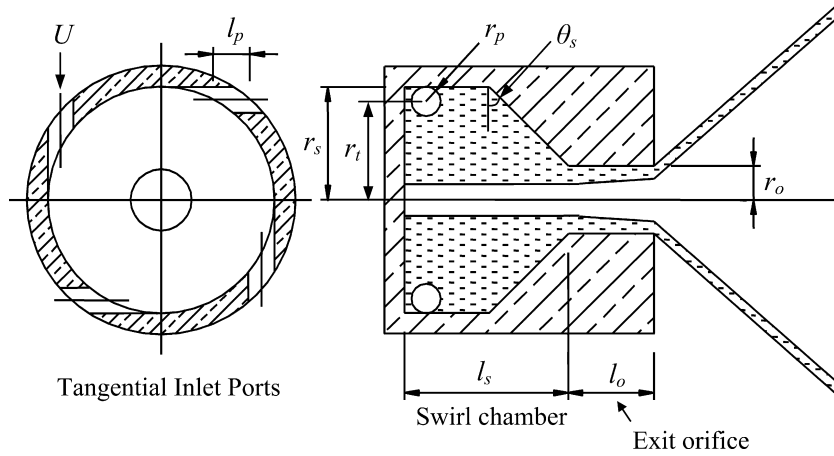
Fig. 1. Geometrical characteristics of simplex nozzle.

2003). At higher injection velocities, turbulent and three-dimensional instabilities, amplified by aerodynamic interactions with the gas, lead to reductions in the azimuthal extent of these ligaments; in the limit direct pinching of droplets from the conical sheet can be observed (Dumouchel, 2008). For this reason, the model described herein will be most applicable to moderate injection speeds wherein sectors of ring-shaped ligaments are formed, and those ligaments subsequently fractionate into drops. This assumption provides for a drastic reduction in computational expense such that full spray simulations are achievable within current computational resources.

The boundary element method (BEM) has been previously applied to investigate instability of free surface and atomization of jets (Hilbing and Heister, 1996, 1998; Heister et al., 1997; Heister, 1997; Rump and Heister, 1998; Yoon and Heister, 2004; Park et al., 2006; Park and Heister, 2006). Park (Park et al., 2006; Park and Heister, 2006) and Yoon (Yoon and Heister, 2004; Park et al., 2006) are credited with development of the elements of the model utilized in the present work. While the BEM formulation is inherently inviscid, a treatment to handle weak viscous effects due to Lundgren and Mansour (1988) has been implemented (Park and Heister, 2006) to provide some consideration for viscous stresses within the fluid.

The BEM has substantial capabilities to simulate highly nonlinear capillary flows including pinching events because all the nodes are placed on the surface of interest. The objective of the present work is to develop simplex nozzle spray distributions from first principles. The model is briefly described in the following section, followed by grid convergence studies, comparisons with measured data, and conclusions from the study.

2. Model description

2.1. Boundary element method

A brief description of the model is provided here in the interest of brevity. Yoon and Heister (2004) provide a complete description of the basic model elements and Park and Heister (2006) provide a detailed description of the incorporation of swirling effects. Under the assumption of inviscid, incompressible, and axisymmetric flow, the flow dynamics are governed by Laplace's equation, $\nabla^2 \phi = 0$. Laplace's equation is transformed to the integral form (Yoon and Heister, 2004) as follows:

$$\alpha\phi(\vec{r}_i) + \int_\Gamma \left[\phi\frac{\partial G}{\partial \hat{n}} - qG\right] d\Gamma = 0 \tag{1}$$

where $\phi(\vec{r}_i)$ is the value of the velocity potential at a point $\vec{r}_i$, q is the differentiation of ϕ with respect to normal vector $\hat{n}$, Γ is the boundary of the domain, α is the singular contribution resulting from integration over the "base point" in question, and G is the free space Green's function for the Laplacian operator. Following Liggett and Liu (1983), the free space Green's function for the axisymmetric Laplacian can be expressed in terms of elliptical integrals of the first and second kinds. Under the assumption that the velocity potential ϕ and the normal velocity q vary linearly over the length of an element, the governing equation yields a linear system of equations relating local ϕ and q values.

The unsteady Bernoulli equation provides a boundary condition at the free surface and relates capillary, hydrostatic, centrifugal, and dynamic pressure forces to the local surface shape. For the swirling flow, modifications are required to account for the pressure gradient created by the swirl. Swirling flows are considered via a superposition of a potential vortex with the base flowfield. If we choose the liquid density (ρ), inlet jet velocity (U), and radius of orifice (r_o) as dimensions, the nondimensional unsteady Bernoulli equation can be written (note that the superscript * is omitted here):

$$\frac{D\phi}{Dt} = \frac{1}{2}|\nabla\phi|^2 - P_g - \frac{\kappa}{\text{We}} + \frac{\text{Bo}}{\text{We}}z \tag{2}$$

with nondimensional parameters as follows:

$$\nabla\phi^* = \frac{\nabla\phi}{U} \quad \phi^* = \frac{\phi}{Ur_o} \quad P_g^* = \frac{P_g}{\rho U^2} \quad t^* = \frac{U}{r_o}t \tag{3}$$

where P_g is dimensionless gas pressure, κ is the local surface curvature and the Weber number (We $= \rho U^2 r_o/\sigma$) and Bond number (Bo $= \rho g r_o^2/\sigma$) appear as governing dimensionless parameters. The total surface velocity $\vec{u}_t$ is computed via a superposition of a potential vortex (ϕ_v, $\vec{u}_v$) with the base axial flow (ϕ, $\vec{u}$). The velocity potential and axial, radial, and circumferential velocity components (u, v, w) can be written as follows:

$$\phi_t = \phi + \phi_v \quad u_t = u + u_v \quad v_t = v + v_v \quad w_t = w + w_v \tag{4}$$

Upon superposition of a potential vortex, combining Eqs. (2) and (4) yields the dimensionless unsteady Bernoulli equation:

$$\frac{D\phi}{Dt} = \frac{1}{2}|\vec{u}_t|^2 - \vec{u}_t \cdot \vec{u}_v - P_g - \frac{\kappa}{\text{We}} + \frac{\text{Bo}}{\text{We}}z \tag{5}$$

The velocity components of the vortex are as follows:

$$u_v = 0 \quad v_v = 0 \quad w_v = \frac{\Gamma_v}{2\pi r} \tag{6}$$

where Γ_ν is vortex strength ($= 2\pi r_t^2 \Omega_t$) and Ω_t is the angular velocity at the location of tangential inlet port. Upon assumption of $U = r_t \Omega_t$, the dimensionless unsteady Bernoulli equation can be expressed using Eqs. (4)–(6):

$$\frac{D\phi}{Dt} = \frac{1}{2}|\vec{u}|^2 - P_g - \frac{\kappa}{We} + \frac{Bo}{We}z - \frac{1}{2}\left(\frac{r_t}{r_o}\right)^2 \frac{1}{r^2} \tag{7}$$

where the Weber number and Bond number are defined as above. The radii r_t and r_o on the RHS of Eq. (7) are defined in Fig. 1. The last term on the RHS of Eq. (7) corresponds to the circumferential pressure force developed by the superposed potential vortex. Inclusion of this effect permits a simulation of swirl produced throughout the flowfield; prior results of Park and Heister (2006) show excellent agreement of measured and predicted cone angles for low viscosity fluids.

The BEM solver returns the velocity potential ϕ or the velocity normal to the local surface ($q = \partial\phi/\partial\hat{n}$) on all computational node points. The first derivative of ϕ along the surface ($\partial\phi/\partial\Gamma$) is computed using a 4th-order centered difference scheme on the surface with the exception of the ends of the domain where forward or backward derivatives are applied. These velocities and the local slope of the surface β can be used in a standard coordinate transformation to provide velocities in axial (z) and radial (r) directions:

$$\frac{\partial\phi}{\partial r} = \frac{\partial\phi}{\partial\Gamma}\sin\beta + q\cos\beta \qquad \frac{\partial\phi}{\partial z} = \frac{\partial\phi}{\partial\Gamma}\cos\beta - q\sin\beta \tag{8}$$

A 4th-order Runge–Kutta time marching scheme is utilized to advance Eqs. (7) and (8) in time. The instantaneous location of surface points is obtained via integration of the surface velocities in Eq. (8). Overall, the scheme has second order accuracy in space and 4th-order accuracy in time. Surface curvature and hence the capillary force, is resolved to 4th-order accuracy via the use of cubic spline fitting of the surface at each instant in time. More details of the numerical scheme are available in Yoon and Heister (2004) and Park and Heister (2006).

2.2. Weak viscous treatment

Lundgren and Mansour (1988) assume in their paper that viscosity in the liquid can be treated as a thin layer of rotational fluid at the free surface. Using this approach, surface velocities can be modified to account for viscous forces. The flow can be divided into two pieces: a rotational thin vortical layer and an irrotational main flow. Thus, the velocity field can be separated into two components:

$$\vec{V} = \vec{u} + \vec{u}' \tag{9}$$

where $\vec{V}$ is the fluid velocity, $\vec{u}$ is the irrotational velocity (inviscid) and $\vec{u}'$ is the vortical velocity (viscous). The irrotational velocity can be expressed as a gradient of a velocity potential ϕ, The vortical velocity can be expressed as the curl of a vector potential ψ:

$$\vec{u} = \nabla\phi \tag{10}$$

$$\vec{u}' = \nabla \times \vec{\psi}, \quad \nabla \cdot \vec{\psi} = 0 \tag{11}$$

where $\vec{\psi} = \psi\hat{\theta}$ and $\hat{\theta}$ is the unit vector in the circumferential direction.

According to Lundgren and Mansour, the vector potential ψ can be expressed as follows:

$$\frac{d\psi}{dt} = -\psi\left(2\frac{\partial^2\phi}{\partial\Gamma^2} + \frac{1}{r}\frac{\partial\phi}{\partial r}\right) + \frac{2}{Re}\frac{\partial q}{\partial\Gamma} \tag{12}$$

and ϕ is expressed correspondingly as follows:

$$\frac{d\phi}{dt} = \frac{1}{2}\left[\left(\frac{\partial\phi}{\partial\Gamma}\right)^2 + (q + u_n')^2\right] + 2\psi\frac{\partial q}{\partial\Gamma} + \frac{2}{Re}\left(\frac{\partial^2\phi}{\partial\Gamma^2} + \frac{1}{r}\frac{\partial\phi}{\partial r}\right) - \frac{\kappa}{We} \tag{13}$$

where u_n' is the normal component of the vortical velocity. u_n' and $d\vec{r}/dt$ are given as follows:

$$\frac{d\vec{r}}{dt} = \vec{u} + u_n'\vec{n}, \quad u_n' = \frac{1}{r}\frac{\partial}{\partial\Gamma}(r\psi) \tag{14}$$

Substituting for the inviscid portion of the velocity field from Eq. (8) gives the axial and radial velocities at each node on the surface:

$$\frac{Dz}{Dt} = \frac{\partial\phi}{\partial\Gamma}\cos\beta - (q + u_n')\sin\beta \tag{15}$$

and

$$\frac{Dr}{Dt} = \frac{\partial\phi}{\partial\Gamma}\sin\beta + (q + u_n')\cos\beta \tag{16}$$

respectively.

This modification is made to incorporate weak viscous effects on $d\phi/dt$ and $d\vec{r}/dt$ replacing the existing boundary conditions on the free surface. The partial derivatives, $\partial^2\phi/\partial\Gamma^2$, $\partial\phi/\partial\Gamma$, and $\partial q/\partial\Gamma$ are calculated using a five-point centered differencing scheme (Hilbing and Heister, 1998). First order differential equations described above are solved by a 4th-order Runge–Kutta time marching scheme with Bernoulli's equation simultaneously. The initial value of the vector potential ψ is set to be zero because the flow is assumed to be initially completely uniform. In addition, the term $\partial^2\phi/\partial\Gamma^2$ is neglected from Eq. (13) following Lundgren and Mansour's suggestion for the high amplitude case due to the existence of a highly distorted surface at the end of the free surface.

2.3. Droplet breakup and formation of satellite drops

Due to the motion of the free surface, nodes tend to bunch in regions of higher curvature. A spline-fit regridding procedure redistributes nodes at constant intervals at the end of each time step in order to maintain overall accuracy. As the surface forms a conical film due to angular momentum conservation, this highly distorted surface near the tip of the film forms annular ring-shaped ligaments. Capillary instabilities result from the nonuniform axial velocity created as fluid flows around the nozzle lip and by viscous interactions with the imposed velocity field. A pinching criterion is used to physically separate ligaments from the parent sheet. A pinching event occurs if the nodes on either side of liquid film lie within 75% of grid spacing (Δs). This criterion is based on the fact that the resultant ligament size was shown to be insensitive to this parameter in prior work (Park and Heister, 2006).

Assuming instantaneous breakup of ligaments into droplets, Ponstein's linear stability theory (Ponstein, 1959) is applied to obtain characteristics of droplets. Ponstein considered the stability of an infinitely long liquid cylinder rotating with circulation Γ_r. His analysis provides a dispersion relation for the growth rate w, of a disturbance with wavenumber k ignoring aerodynamic interactions with the gas phase:

$$w^2 = \left[\frac{\sigma}{\rho a_r^3}(1 - k^2 a_r^2) + \left(\frac{\Gamma_r}{2\pi a_r^2}\right)^2\right](ka_r)\frac{I_1(ka_r)}{I_0(ka_r)} \tag{17}$$

where a_r is the radius of the rotating liquid column and I_0 and I_1 are the modified Bessel functions of zeroth and first orders. This dispersion equation is solved to determine the most unstable wave number k_{max} corresponding to the maximum growth rate, w for a given ring geometry and circulation. Upon the assumption that Ponstein's approach on the rotating liquid column can be applied to the vortex ring, i.e., that the ring radius a_r is much smaller than the overall radius of the ring itself. This assumption implies $ka_r \ll 1.0$ for the validity and ligament size results confirmed that this assumption is quite valid for the cases studied. In the present context,

ring-shaped ligaments maintain a small rate of rotation at pinchoff due to the multidimensional velocity field and unbalanced capillary forces at the pinching event. In general, the capillary term (first term on RHS of Eq. (17)) tends to dominate in the computation of the most unstable wavenumber for a given ring-shaped ligament.

Park et al. (2006) investigated nonlinear corrections to the Ponstein's result by considering droplet formation from a rotating liquid column. Nonlinear simulations were conducted for a range of wavelengths and as with Rayleigh jets, a given wave tended to fractionate into two drops, main and satellite. Interestingly, the researchers found that the ratio of the main/satellite drop sizes was nearly invariant regardless of wavelength or swirl strength, thereby providing a very simple correction to Ponstein's linear theory. The predicted main drop size from the BEM calculation corresponds to 99% of the drop size obtained from Ponstein's theory and the satellite drop size corresponds to 31% of the drop size obtained from Ponstein's theory over a variety of swirl strengths. This result is implemented in a post-processing code for SMD and drop size distribution.

3. Results and discussion

3.1. Computational mesh

The initial computational mesh and geometric parameters for the simulation of a pressure-swirl atomizer is illustrated in Fig. 2. All variables except the width of inlet port w_p should be given for the calculation. Most practical configurations utilize a discrete number (generally 4–6) of tangential inlet ports that makes for a three-dimensional object in the inlet region. For 2-D axisymmetric calculation, an equivalent axisymmetric inlet slot is used assuming similar inlet areas. Therefore, the width of inlet slot, w_p, can be calculated as follows:

$$w_p = \frac{1}{2}\frac{n_p r_p^2}{r_s} \tag{18}$$

Parametric studies were performed with various inlet areas, and results showed that the flow conditions far downstream (in exit orifice, for instance) are insensitive to this parameter (Park,

2008). Unfortunately, most prior studies do not stipulate l_p and z_p values. Thus, l_p and z_p are chosen within reasonable bounds based on the same parametric studies on the inlet areas.

The initial grid system is constructed with given geometric parameters. It is noted that the grid system is changed due to the propagation of free surface to outside. The grid system on the free surface is re-constructed at each time step using a cubic spline interpolation with a given grid spacing Δs. Therefore, the number of nodes on free surface increases as the conical sheet lengthens and decreases when a ligament is pinched off.

All geometrical parameters are nondimensionalized by the exit orifice radius r_o. For the mesh shown in Fig. 2, a total of 105 fixed node points are used to describe the wall geometry. The contact point between the wall and the free surface inside the injector is required to be treated differently from other node points in order to simulate air-core inside injector. This corner is treated as a moving grid point. As this corner moves, the grid space along the wall is stretched in order to compensate the shifted distance. Therefore, gas core radius inside injector appears naturally.

A fictitious hemispherical cap is assumed for the end of the free surface. This cap is shed with the first ligament pinching-off event and after several pinching-off events memory of the initial condition is lost.

3.2. Spray characterization parameters

Fig. 3 illustrates the geometrical parameters describing the film formed in the nozzle of a simplex atomizer. Due to the swirl in swirl chamber produced from the flow coming through tangential inlet ports, the flow forms a thin film and therefore, forms an air core along the entire injector. The parameters, r_{a1}, r_{a2} and r_{a3}, represent air core radius in the swirl chamber, at the entrance of orifice, and at the exit of orifice respectively. The parameters, t_1 and t_2, represent film thickness at the entrance of orifice and at the exit respectively. The half cone angle θ is defined as the angle from the axis of symmetry to the first order polynomial fit to the upper surface here.

The SMD is calculated for the statistical characteristic of a simplex nozzle. Because a fictitious hemispherical cap at the end of the conical sheet is utilized for the initial shape of free surface, drops
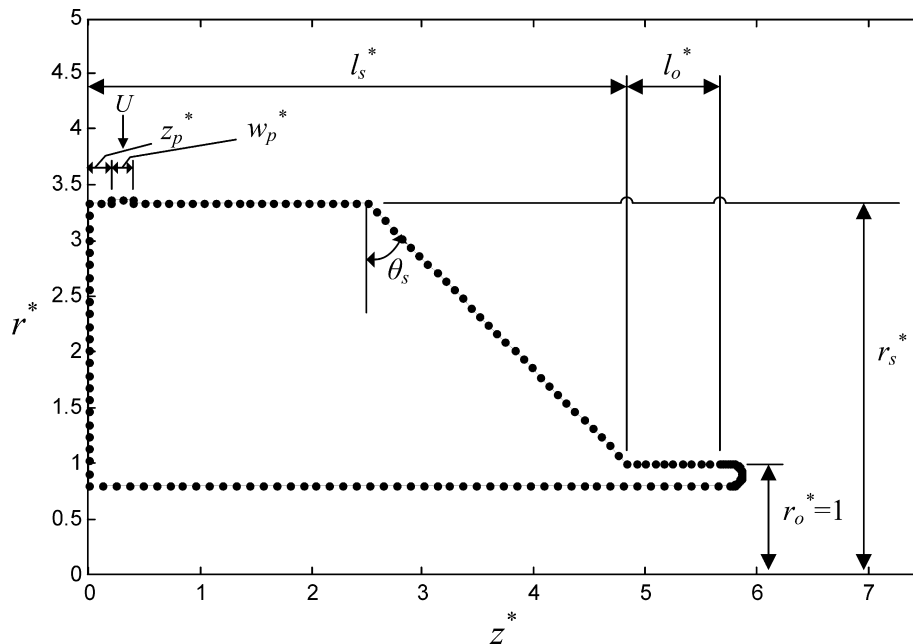

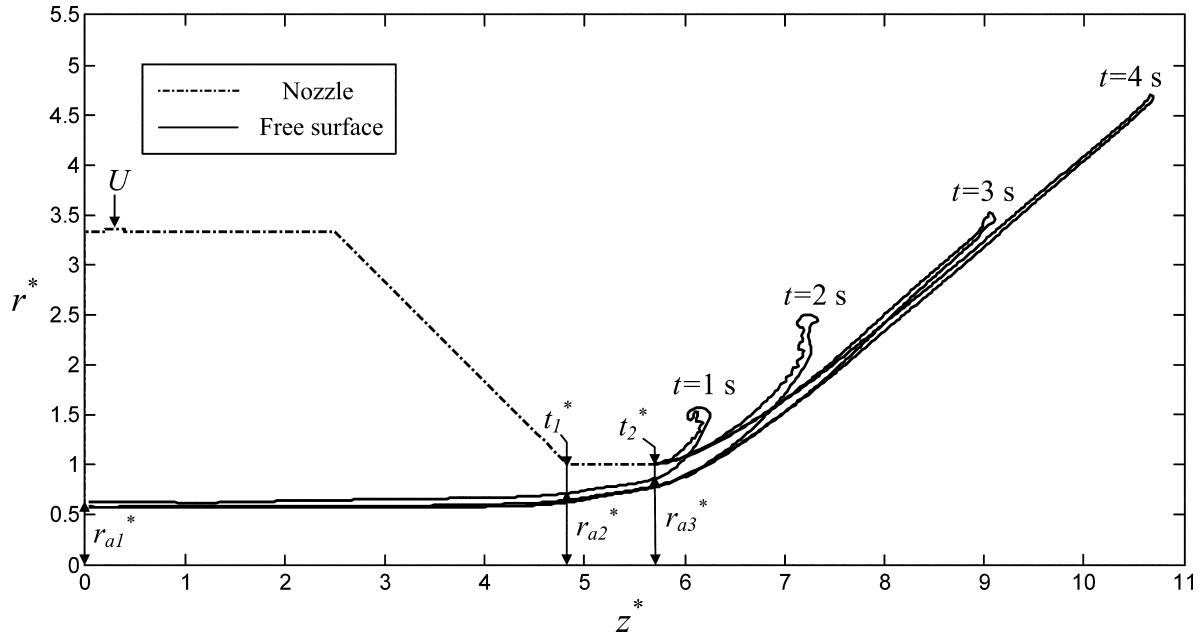**Fig. 2.** Schematic of the grid system for a simplex nozzle.

Fig. 3. Critical characteristic parameters for a simplex nozzle and free surface time evolving from 1 s to 4 s.

only collected after the flow is fully developed are used for the SMD and drop size distribution. The SMD from original diameter of droplets is calculated using the definition:

$$\text{SMD} = \frac{\sum ND^3}{\sum ND^2} \qquad (19)$$

where N is the number of drops and D is the diameter of drops. Because the simulation gives the exact size of drops at each pinching event, the effect of drop size range, ΔD_i, can be removed from the calculation. Experimentally, drop size distributions are constructed by adding the number of drops within the given bin sizes which are determined by the measuring device. For example, Malvern particle sizer with 600 mm focal length lens used in Cousin et al.'s (1996) experiments is able to detect drops whose diameter ranges from 11.6 μm to 1128 μm. The focal length of lens on the receiver of Malvern particle sizer determines the detectable diameter ranges and corresponding bin sizes.

As the model does not include chaotic behavior due to turbulence or geometric imperfections, it tends to create a very narrow distribution when compared with the experimental results. In addition, the treatment of the ring breakup process in the present work removes azimuthal variations that are observed in the experimental results at the injection velocity range of interest. For these reasons, other authors developing spray models have utilized a distribution function (Sellens, 1989; Ahmadi and Sellens, 1993; Cousin et al., 1996) to better represent results in the light of experimental data which presumably include the chaotic processes noted above. As computational power grows, the additional resolution will permit the consideration of the additional factors, but in the present environment the existing modeling tools simply cannot account for all the physical processes pertinent to spray development in a high-speed atomizer. As experimental distributions are generally fit using similar mechanisms, there is additional motivation to put our results in this form. For these reasons, we chose to fit data using a log-normal distribution function as was done by Durst and Bhatia (1989) and Ahmadi and Sellens (1993).

$$\text{SMD}_f = \frac{\int_0^\infty D^3(dN/dD)dD}{\int_0^\infty D^2(dN/dD)dD} \qquad (20)$$

where dN/dD is a fitted drop size distribution function (log-normal) to given drop size data.

3.3. Grid convergence study

Park and Heister (2006) were able to simulate the grid spacings ranging from 0.024 to 0.040 using Successive Over Relaxation (SOR) method for matrix inversion. Results showed a reduction of SMD with decreased grid spacing such that results were not sufficient to confirm the grid convergence. To demonstrate the grid convergence on SMD, smaller grid spacings were desired. Matrix inversion using the ScaLAPACK (Blackford et al., 1997) within the linear system solver was implemented as a precursor to the present study. Details of this formulation can be found in Park (2008). Implementation of the ScaLAPACK matrix inversion software made it possible to simulate smaller grid spacing cases giving better grid convergence on SMD. The test conditions used for the grid convergence study are given in Table 1. The grid spacing varies from 0.016 to 0.032 with increments of 0.004. The simulation time is from 0 s to 10.1 s. The code ran with a constant grid size from the beginning in order to reduce the possibility of perturbations in grid size affecting results. The computed flow characteristics

Table 1
Geometry and flow conditions for grid convergence test.

Parameters	Dimensions
r_s (mm)	2.0
l_s (mm)	2.9
θ_s (°)	45
r_o (mm)	0.6
l_o (mm)	0.5
r_p (mm)	0.4
l_p (mm)	0.018
z_p (mm)	0.12
n_p	3
w_p (mm)	0.12
U (m/s)	5.13
We	447.9
Bo	0
Re	1861.1

Table 2
Characteristic parameters according to the grid size.

Δs	0.032	0.028	0.024	0.020	0.016
θ (°)	37.8	38.3	38.3	38.2	38.3
t_1 (mm)	0.225	0.224	0.225	0.225	0.225
t_2 (mm)	0.138	0.138	0.138	0.138	0.138
r_{a1} (mm)	0.346	0.346	0.346	0.346	0.346
r_{a2} (mm)	0.375	0.376	0.375	0.375	0.375
r_{a3} (mm)	0.462	0.462	0.462	0.462	0.462
SMD (µm)	73.3	62.7	53.4	49.0	46.9
SMD_f (µm)	113.2	102.3	81.0	71.5	58.5
N_D[a]	12,294	17,688	19,215	29,251	40,596

[a] N_D is the number of sampled drops after the flow is fully developed.

are summarized in Table 2. Half cone angle, film thickness, and air core radius values converge rapidly, while SMD values are more challenging to gain convergence due to the small structures evolved at the tip of the conical sheet. However, SMD values are converging to a limiting value as depicted in the plot of this parameter vs. the square of the step size in Fig. 4. When Δs goes to zero, the extrapolated SMD value is approximately 45 µm. Therefore, a very fine grid spacing is required to get meaningful statistical properties.

3.4. Code validation – statistical properties

The simulation code for a simplex nozzle is validated here against experimental results provided by Cousin et al. (1996). Their experimental conditions are provided in Table 3. The experiment utilized four injectors with varying orifice radius all driven with a pressure difference, $\Delta P = 10$ bar. The researchers provided the results of cone angle, SMD, and drop size distribution. The fluid used in experiment is water.

Due to computational constraints, the grid spacing used for injector J_1 is 0.024, 0.020 for injector J_2, and 0.016 for injector J_3 and J_4. Using $\Delta s = 0.016$ may be the best choice for better converged statistical properties, but large computational time is required for this small Δs. For the simulation of injector J_1, approximately 30.3 days are taken to obtain a result up to $t = 8$ s. In case of J_2, 46.2 days are spent for the simulation up to $t = 8$ s. 45 days are spent for the simulation of J_3 up to $t = 8$ s and 15.8 days

are spent for the simulation of J_4 up to $t = 10$ s. All simulations are performed on our current 2.4 GHz AMD Opteron Dual Processor HPC cluster, two processors per node.

Half cone angles and SMD values from experiments and simulations are compared in Table 4. The number of collected droplets for the statistical analysis is over 40,000 for each injector. For the simulations, SMD_f is calculated from the number distribution curve constructed from the same bin sizes corresponding to a 600 mm focal length lens on a Malvern particle sizer. These bin sizes were chosen to be consistent with the measurements of Cousin et al. (1996). The half cone angles calculated using BEM code show a good agreement with Cousin et al.'s experimental results for all four injectors while the SMD from simulations is 30–40% smaller

Table 3
Geometry and inflow conditions for the simulation of Cousin et al.'s experiment.

Injector no.	J_1	J_2	J_3	J_4
r_s (mm)	3.5	3.5	3.5	3.5
l_s (mm)	5	5	5	5
θ_s (°)	90	90	90	90
r_o (mm)	0.5	0.6	0.75	1.0
l_o (mm)	1	1	1	1
r_p (mm)	0.5	0.5	0.5	0.5
l_p (mm) ($l_p^* = 0.03$)	0.015	0.018	0.0225	0.03
z_p (mm) ($z_p^* = 0.2$)	0.1	0.12	0.15	0.2
n_p	6	6	6	6
w_p (mm)	0.214	0.214	0.214	0.214
U (m/s)	3.578	4.508	5.534	7.752
We	87.806	167.259	315.073	824.328
Bo	0	0	0	0
Re	2001.118	3025.503	4642.617	8671.140

Table 4
Comparison of experimental results and simulation results for the simulation of Cousin et al.'s experiment.

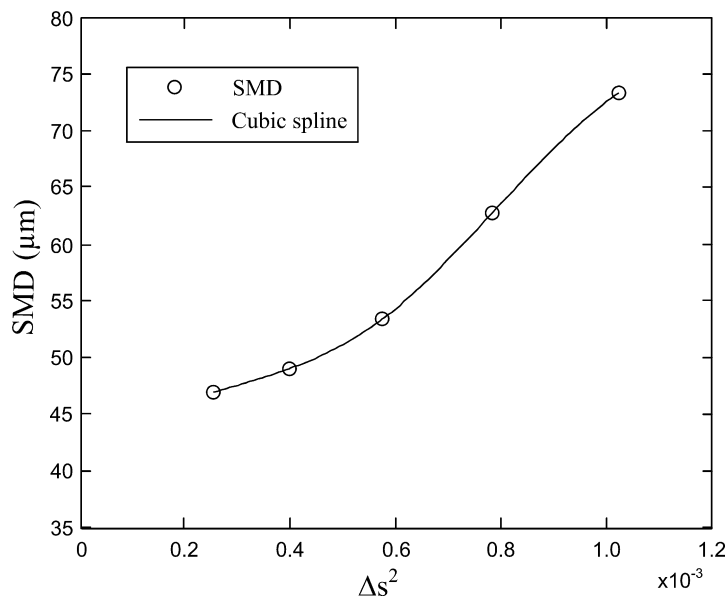|	Experiment		Simulation		
	θ (°)	SMD (µm)	θ (°)	SMD (µm)	SMD_f (µm)
J_1	30	102	29.5	51.0	69.7
J_2	29	118	32.3	52.4	70.9
J_3	34	114	35.4	58.1	73.1
J_4	36	135	39.3	71.3	88.8

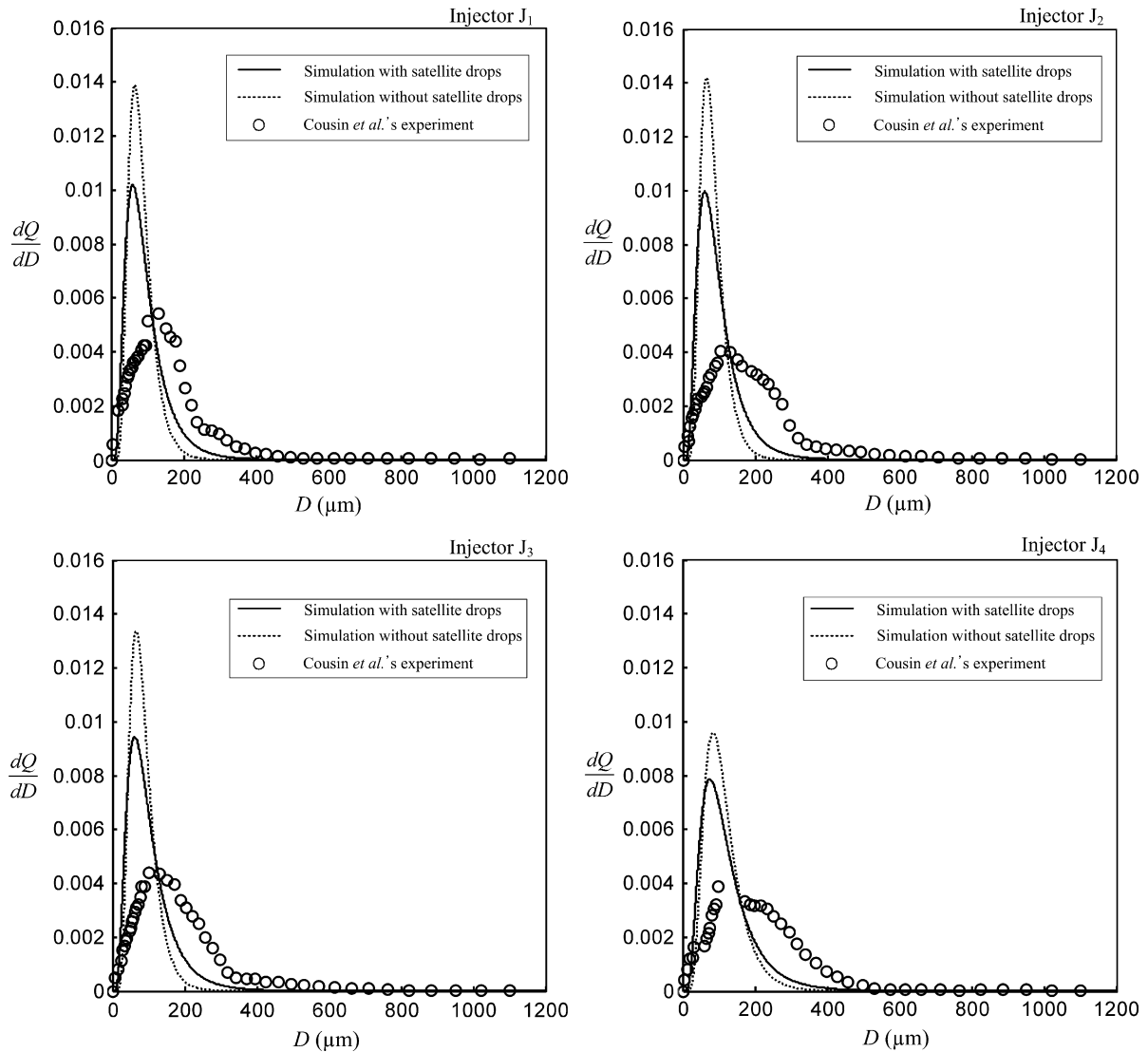**Fig. 4.** The SMD vs. square mesh spacing.

Fig. 5. Comparison of volumetric distribution between experimental result and simulation results with and without satellite drops for Cousin et al.'s nozzles J_1, J_2, J_3 and J_4.

than the experimental measurements for all cases. This difference mainly attributed to the treatment of satellite drops theorized to come from ring ligament atomization in the model.

One thing should be noted here is that Δs used in J_1 and J_2 is 0.024 and 0.020 respectively. As it is shown in grid convergence section, SMD is somewhat related to the grid spacing at these levels. When large Δs is used in simulation, corresponding SMD is bigger than the converged SMD with small Δs. Therefore, SMD corresponding to 0.024 and 0.020 is bigger than SMD corresponding to 0.016. This is the reason why SMD on J_1 and J_2 are similar to each other. So, it can be expected that SMD on J_1 and J_2 will be smaller than current value and the tendency of SMD change between injectors follows the tendency of SMD change in experimental results if 0.016 is used for Δs in J_1 and J_2. The overall tendency of SMD change is well agreed with the experimental results except the tendency between J_2 and J_3.

Fig. 5 presents a comparison of volume PDFs from the model with the experimental results of Cousin et al. (1996). In general, the model shows a much narrower distribution due to the assumption of uniform atomization of the ring-shaped ligaments (per Ponstein) and the presence of nonaxisymmetric structures along the periphery of the atomizing surface. Model results show a peak in the distribution curves at significantly smaller droplet sizes than those in the measurements. It is clearly seen that the model overestimates the smaller droplets relatively to the measurements. Including the satellite drop treatment of Park et al. (2006) shows a lower peak at a slightly smaller drop size (solid curve in Fig. 5 vs. the dashed curve). The treatment of ring ligament breakup provides a lower bound on the drop size distribution in that finite-length ligaments would have some time to collapse in the azimuthal direction prior to atomization into drops. Clearly this is an area worthy of further study as it is likely the largest contributor to the disparity between the two sets of results.

It should be noted here that Cousin et al.'s volume distributions also have an inflection in relatively small drop size region of the distribution curves (injector J_4 shows this inflection most prominently). Van Der Geld and Vermeer (1994) have shown that this sort of behavior can be attributed to the presence of satellite droplets as it is indicative of tendency toward a bimodal distribution with the satellite droplet peak substantially suppressed relative to the primary peak in this case. The following two sections provide additional discussion on this issue.

3.5. Effect of satellite drops on SMD and drop size distribution

The effect of satellite drops on statistical properties is investigated in this section. Based on the investigation of Park et al. (2006) on the formation of droplets from a rotating column, the SMD value and drop size distribution without satellite drops are compared to the results with satellite drops for the injector used in grid convergence study. Ignoring the formation of satellite drops, statistical properties are obtained directly from Ponstein's linear instability theory. Considering the formation of satellite drops, main drops are corresponding to 99% of Ponstein's result and satellite drops are corresponding to 31% of Ponstein's result as described above.

The comparisons of SMD are provided in Table 5 for a wide range of Δs. Addition of the satellite drops tends to reduce SMD by about 10% for the case shown. Fig. 6 depicts the effects on the overall drop size distribution curve for the 0.016 grid spacing. The drop size distribution curve is shifted significantly to the left due to the presence of satellite drops. Due to the small size/volume of the satellite drops, this effect is much less pronounced on a volumetric PDF basis as indicated in Fig. 5.

While in principle the BEM result gives the exact size of drops at each pinching event, comparison against experimental data necessitates the use of similar bin sizes (ΔD_i value). The drop size distribution of the simulation can be created for a variety of different bin sizes. Considering bin size data from Malvern particle sizer, the drop size distributions are illustrated in Fig. 7 for 100 and 800 mm focal length. The Fig. 7 is constructed from the data ob-

tained from the $\Delta s = 0.016$ case of the nozzle in grid convergence study. A total of 74,567 and 56,110 droplets are included in 100 and 800 mm focal length distribution respectively.
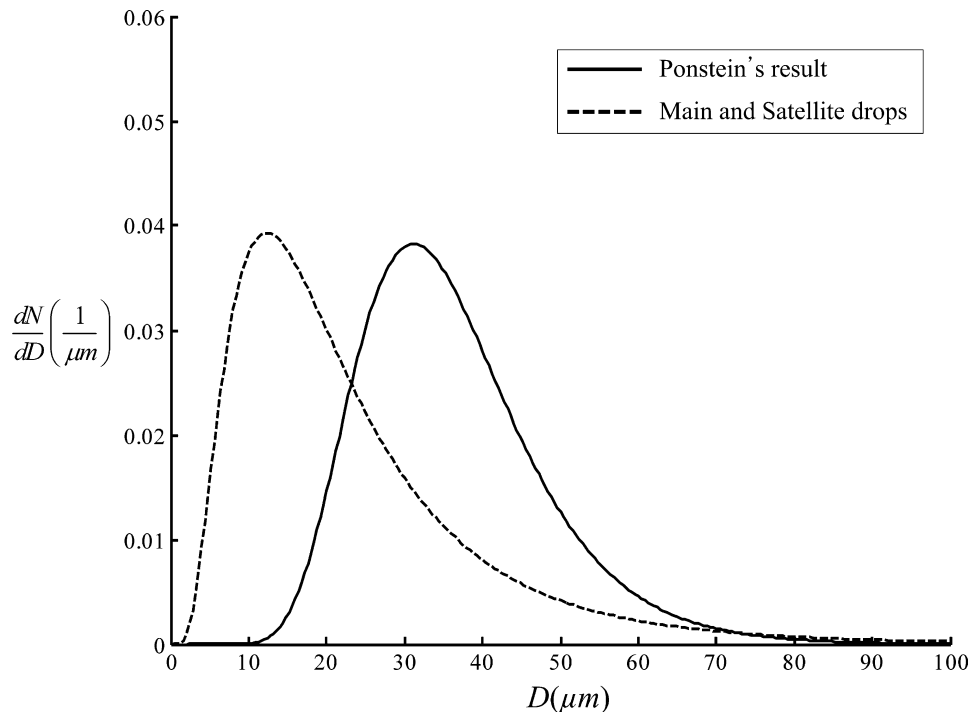
Fig. 7 results show changes in distributions depending on the ΔD_i value employed. The simulations show many drops below the 15.4 μm threshold. The small size also makes it likely that viscous effects may inhibit their appearance. The Ohnesorge number for a 10 μm drop in this flow field is 0.088 indicating that we are near a region where viscosity is known to affect secondary atomization.

Considering ΔD_i value from Malvern in the simulation result, 100 mm focal length case will be suitable because the droplets exist below 160 μm. The width of droplet existing range being relatively small, the satellite drops can have significant effects on the overall shape of the number distribution curve and consequently the distribution curve slightly moves to the right as focal length getting bigger.

The histogram is substantially different than the log-normal curvefit as shown in Fig. 7 due to the large amount of small droplets below 15.4 μm threshold. In addition, the simulation creates large amount of drops in very small ranges (near 10, 24, and 38 μm) as it can be seen from the histogram. This result stems from the modeling of the ring breakup process using Ponstein's analysis and subsequent satellite drop analysis of Park et al. (2006). The formation of satellite drops is a nonlinear phenomenon. In addition, the existence of sub-satellite drop formation has also been suggested by Van Der Geld and Vermeer (1994) for the ligaments formed in liquid sheet atomization; existence of this third drop size category would reduce the height of the peak coming from satellite drops in Fig. 7. Establishing the number and size of satellite drops formed in ring ligament atomization remains an open research issue as suggested earlier.

3.6. The bimodality of drop size distribution

Until now, many studies have assumed that the drop size distribution can be characterized from a unimodal distribution such as

Table 5
Comparison of SMD of Ponstein's result and main and satellite drops for the injector in grid convergence study.

Δs	0.032	0.028	0.024	0.020	0.016
SMD (main and satellite drops)	73.3	62.7	53.4	49.0	46.9
SMD (Ponstein's result)	78.93	67.53	57.51	52.76	50.52

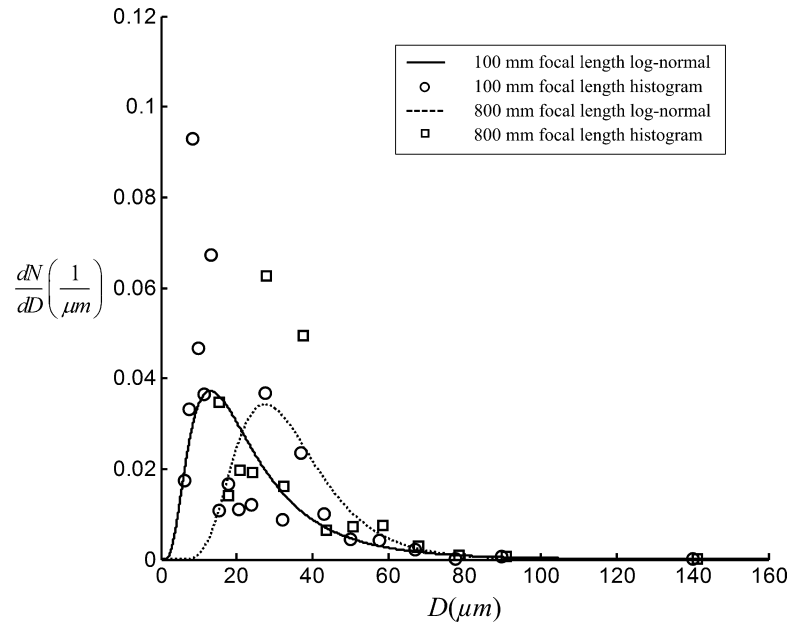**Fig. 6.** Comparison of number PDF of Ponstein's results and main and satellite drops.

Fig. 7. Number PDF distribution of main and satellite drops for the simplex nozzle of grid convergence study with 100 and 800 mm focal length Malvern bin size data.

log-normal or log-hyperbolic, etc. However, oftentimes the size of satellite drops is relatively small so that detection by measuring device may be difficult as a large range of sizes is typically created in high-speed sprays. This could lead to underestimate the number of satellite drops and the corresponding distribution shows a unimodal shape. For combustion problems, this is an important issue as ignition can chemical kinetics behavior may be highly dependent on very small drops that vaporize rapidly in a combustor environment. The bimodality of drop size distribution due to the satellite drops has been already indicated by Van Der Geld and Vermeer (1994) for the ligament from the liquid sheet (nonswirling). They also show the result of Sellens' (1987) experimental result showing the bimodality of the distribution.

Our simulation results show a strong bimodality as shown in the 100 mm focal length histogram of Fig. 7. The first peak point is located at around 10 μm corresponding to satellite drops formed in ring ligament atomization events. The second peak point contributed by main drops is located at around 30 μm. Because there is no theoretical basis for measuring bimodality, it is difficult to determine which distribution curve shows a good agreement with the given data set. So, the way to compare errors produced after the data is fitted to bimodal distribution curve and log-normal distribution curve is used for checking bimodality. The bimodal distribution function is given as follows:

$$f(D) = \frac{P}{\sqrt{2\pi}s_{n,1}}e^{-\frac{1}{2}\left(\frac{D-\bar{D}_1}{s_{n,1}}\right)^2} + \frac{1-P}{\sqrt{2\pi}s_{n,2}}e^{-\frac{1}{2}\left(\frac{D-\bar{D}_2}{s_{n,2}}\right)^2} \tag{21}$$

This bimodal distribution function represents the mixture of two different normal distributions. The variables, $s_{n,1}$ and $\bar{D}_1$, represent a deviation and mean value for first normal distribution respectively and $s_{n,2}$ and $\bar{D}_2$ are for second normal distribution. The variable P is the value for the normalization. The error for the fitted curve is defined as follows:

$$E = \left(\sum(Y_i - y_i)^2\right)^{\frac{1}{2}} \tag{22}$$

where Y_i is the actual data and y_i is the data on the fitted curve.

The unknown parameters in a bimodal distribution function are found by the unconstrained nonlinear optimization implemented

in MATLAB. Because the unconstrained nonlinear optimization method can have several local optimums, it is pretty important to check that the converged solution is consistent with a desired shape of function.

Fig. 8 shows log-normal and bimodal distributions fitted to 100 mm focal length histogram of Fig. 7 including main and satellite drops. The peak values are significantly different from each other. The first peak point value in histogram is around 0.09 at 10 μm. This point appears in bimodal distribution fitting and the value is slightly smaller than the value from the histogram. In case of log-normal fitting, it shrinks to small value to be balanced with other small values which are placed by peak value. The second peak point value which is placed at around 30 μm in histogram is underestimated in log-normal fitting.

The error for bimodal distribution is 0.06122 and the error for log-normal distribution is 0.09691. Therefore, it can be concluded that the original data set for this case is slightly closer to bimodal distribution than unimodal distribution. The bimodal results are a direct consequence of the assumed presence of satellite drops formed during the ligament atomization process as modeled in this work. As the annular ligaments are longer than finite-span ligaments observed at the higher injection pressures, we presume that the model would overpredict the number of satellite drops as a finite-span ligament will have some time to collapse prior to atomization (depending on the amount of initial diliation of course). In combustion applications, the smallest drops can influence ignition and kinetics performance and are therefore of interest in these fields of study. In spray deposition processes these drops are typically of lesser concern as they carry only a very small fraction of the mass of the spray. Clearly this is an area ripe for further study and improvement of the ligament treatment within the model.

3.7. Quasi-three dimensional spray evolution

One of the true values of a comprehensive simulation such as that described in this study is that it permits the spatio-temporal evolution of the spray to be simulated while many prior/existing models simply provide drop sizes and no spatial evolution data. Drop statistics are important for establishing atomizer performance, but the location and velocity of the drops within the
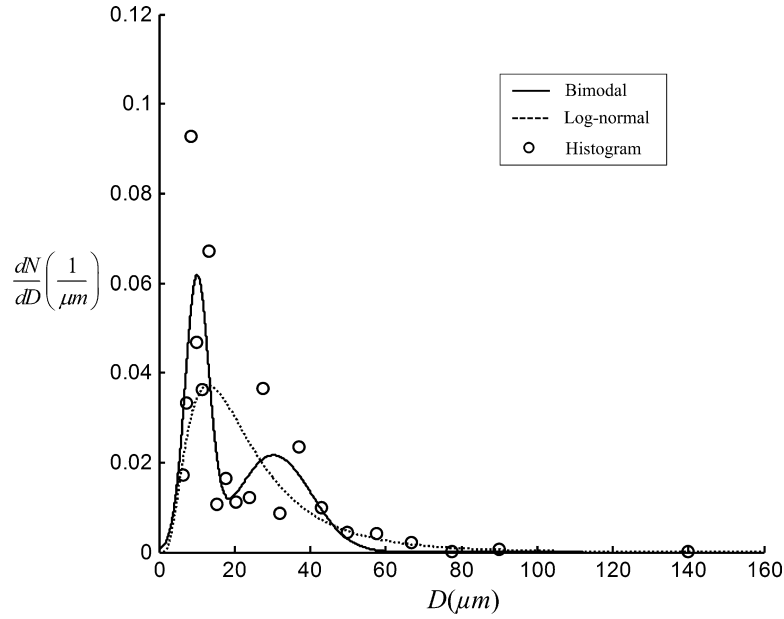
Fig. 8. Number PDF distribution of main and satellite drops for 100 mm focal length fitted to bimodal and log-normal distribution.

flowfield is critical to applications where mixing is important. For this reason, a drop tracking algorithm was added to the model to enable this capability. The algorithm is not fully coupled with the gas-phase and a simple stagnant gas is assumed to compute the local droplet drag (Hilbing and Heister, 1998). Assuming that droplets shed from ring-shaped ligaments are uniformly distributed about the periphery and that their initial velocity is the same as the centroid of the ligament permits an initial condition for a quasi-3-D simulation.

Newton's 2nd law is applied in the tracking scheme to describe the motion of a droplet against aerodynamic drag force. The governing equation for the motion of a droplet is as follows:

$$m_D \frac{d\vec{u}_D}{dt} = C_D \frac{1}{2} \rho_g |\vec{u}_D|^2 A_D \tag{23}$$

where A_D is the projected area of a droplet ($\pi D^2/4$), m_D and $\vec{u}_D$ is droplet mass and velocity, respectively. The drag coefficient C_D is given by Hwang et al. (1996):

$$C_D = \begin{cases} 24/\text{Re}_D \left(1 + \frac{1}{6}\text{Re}_D^{2/3}\right) & \text{Re}_D \leqslant 1000 \\ 0.424 & \text{Re}_D > 1000 \end{cases} \tag{24}$$

where $\text{Re}_D = U_R D \rho_{\text{air}}/\mu_{\text{air}}$ where U_R is a relative velocity between droplet and air.

The ordinary differential equations (23) are integrated in time to obtain instantaneous droplet velocity components and position using a 4th-order Runge–Kutta time marching scheme. Collisions between droplets, vaporization, and the velocity of air (momentum interchange between fluids) are neglected. After the droplet tracking is completed, individual droplet tracks are then assembled in Tecplot. Each droplet represents one zone and the number of zones which can be presented at one time is limited to 32,700 by Tecplot (Tecplot User's Manual). Therefore, droplets are divided into several sets containing the drops less than 32,700 and then each set is drawn in a picture frame and the sets for the drops generated at the same simulation time are integrated into one frame. Due to this limitation, satellite drops are not included in the visualization.

The flow field produced by Cousin et al.'s injector J_4 is presented in Fig. 9. As mentioned above, the total simulation time for this

injector on our current 2.4 GHz AMD Opteron Dual Processor HPC cluster, two processors per node, is 15.8 days. The computational time of post-processing is approximately 1 day on 1.86 GHz Intel Xeon Quad Processor workstation generating a data file for each frame of 24 frame/s movie. Larger droplets are generated in the startup transient regions and contribute significantly to a "bushier" spray appearance early in the visualization. At $t = 10$ s, some of these larger drops are evident on the outer periphery of the spray. At this time, a total number of droplets contained in the picture is about 82,000. While the computational environment is not such that spray simulations of this nature will be a routine part of an atomizer design, the ever-increasing computational resources may soon make such simulations practical in a design environment.

4. Conclusions

An axisymmetric boundary element method, in concert with a nonlinear secondary atomization simulation of ring-shaped ligaments has been developed to provide first-principles spray simulations of the pressure-swirl atomizer. Ponstein's linear stability analysis of a rotating column is used to assess the number of droplets formed from each ligament. A nonlinear analysis of this flow field leads to a prediction of satellite droplet sizes formed from these presumed pinching events. Grid convergence has been demonstrated on the basis of SMD for typical injector performance range.

The model included a weak viscous treatment and accounted for satellite drop formation and was validated against experimental results for air core radius, half cone angle, SMD, and drop size distribution. Film properties and cone angle agree well with measurements while predicted SMD values are of the order of 30–40% lower than the experimental values. The SMD values are significantly influenced by the annular ring breakup via Ponstein's analysis as observations indicate ligaments that are finite in azimuthal extent. The presumed presence of satellite droplets lead to bimodal-type distributions of the simulated drop populations. Their presence leads to a 10% reduction in SMD, i.e., the predictions would improve to 10–20% accuracy if the satellite drops were neglected. As the ligament treatment does not allow for ligament col-
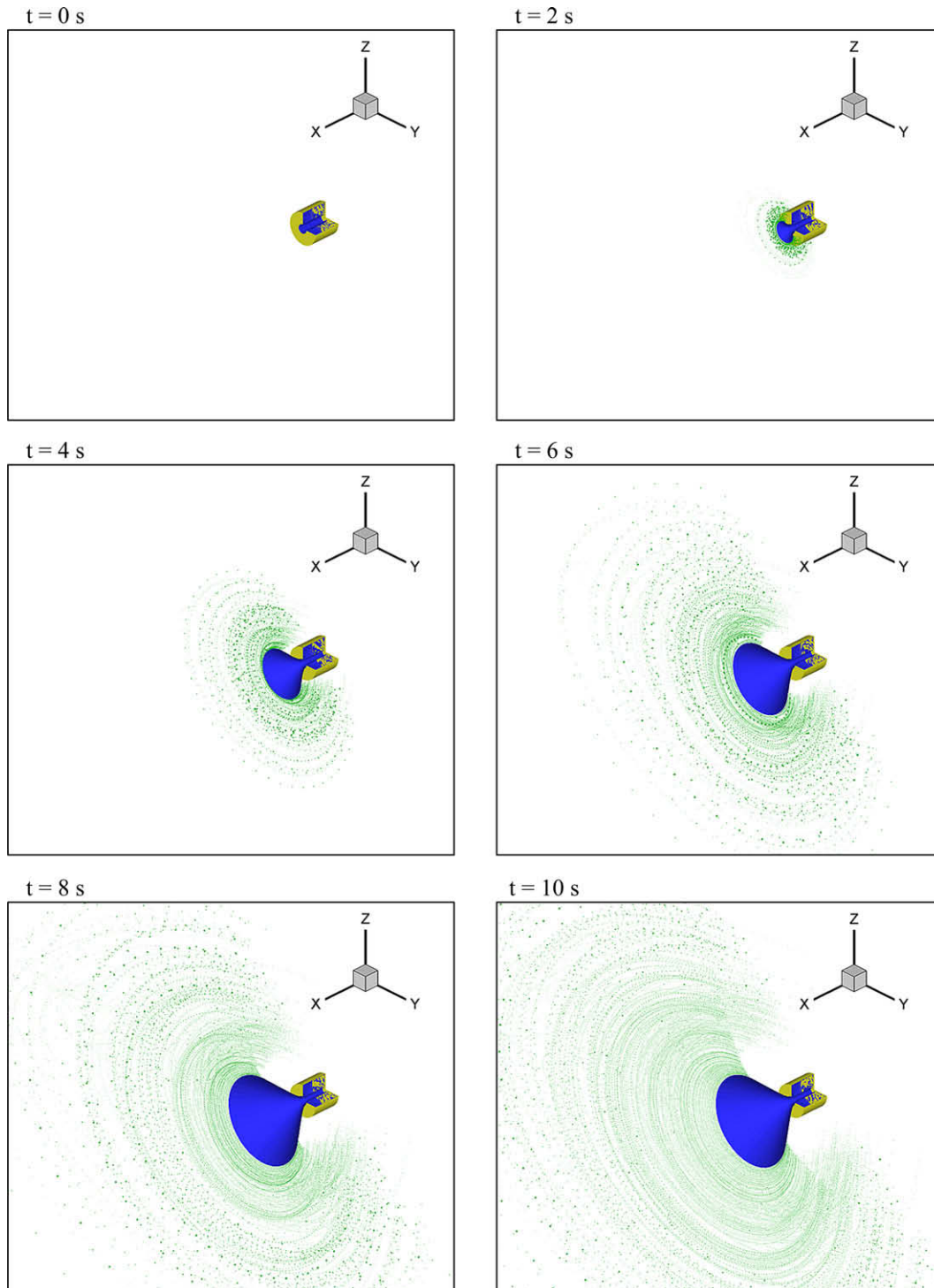
Fig. 9. Spray simulation for Cousin et al.'s injector J_4, total N_D at $t = 10$ s is about 82,000 (N_D is the number of drops).

lapse the model results likely provide an upper bound on the number of satellite drops that may be present. This is clearly an area that would warrant additional investigation.

Finally, a quasi-3-D spray simulation was produced by assuming rings are instantaneously pinched into droplets that are equally distributed azimuthally. Drops are tracked neglecting collision and drag is estimated assuming a locally stagnant gas. A resulting simulation of over 80,000 droplets provides a full spatio-temporal evolution of a spray emanating from a pressure-swirl atomizer at realistic operating conditions.

Appendix A. Supplementary material

Supplementary data associated with this article can be found, in the online version, at doi:10.1016/j.ijmultiphaseflow.2009.09.004.

References

Ahmadi, M., Sellens, R.W., 1993. A simplified maximum-entropy-based drop size distribution. Atomization and Sprays 3, 291–310.

Bayvel, L., Orzechowski, Z., 1993. Liquid Atomization. Taylor & Francis, Washington, DC.

Bazarov, V.G., Yang, V., 1998. Liquid-propellant rocket engine injector dynamics. Journal of Propulsion and Power 14, 797–806.

Blackford, L.S., Choi, J., Cleary, A., D'Azevedo, E., Demmel, J., Dhillon, I., Dongarra, J., Hammarling, S., Henry, G., Petitet, A., Stanley, K., Walker, D., Whaley, R.C., 1997. ScaLAPACK Users' Guide. Society for Industrial and Applied Mathematics Press, Philadelphia.

Cousin, J., Yoon, S.J., Dumouchel, C., 1996. Coupling of classical linear theory and maximum entropy formalism for prediction of drop size distribution in sprays: application to pressure-swirl atomizers. Atomization and Sprays 6, 601–622.

Dumouchel, C., 2008. On the experimental investigation on primary atomization of liquid streams. Experiments in Fluids 45, 371–422.

Durst, F., Bhatia, J.C., 1989. Comparative study of some probability distributions applied to liquid sprays. Particle & Particle Systems Characterization 6, 151–162.

Han, Z., Parrish, S., Farrel, P.V., Reitz, R.D., 1997. Modeling atomization processes of pressure-swirl hollow-cone fuel sprays. Atomization and Sprays 7, 663–684.

Heister, S.D., 1997. Boundary element methods for two-fluid free surface flows. Engineering Analysis with Boundary Elements 19, 309–317.

Heister, S.D., Rutz, M., Hilbing, J.H., 1997. Effect of acoustic perturbations on liquid jet atomization. Journal of Propulsion and Power 13, 82–88.

Hilbing, J.H., Heister, S.D., 1996. Droplet size control in liquid jet breakup. Physics of Fluids 8, 1574–1581.

Hilbing, J.H., Heister, S.D., 1998. Nonlinear simulation of a high-speed viscous liquid jet. Atomization and Sprays 8, 155–178.

Hwang, S., Liu, Z., Reitz, R.D., 1996. Breakup mechanisms and drag coefficients of high speed vaporizing liquid drops. Atomization and Sprays 6, 353–376.

Kim, D., Yoon, Y., Han, P., 2003. Effect of flow condition and geometry on flow characteristics of a swirl injector. In: ILASS Americas 16th Annual Conference, Monterey, CA.

Lefebvre, A.H., 1989. Atomization and Sprays. Taylor & Francis, Washington, DC.

Liao, Y., Sakman, A.T., Jeng, S.M., Jog, M.A., Benjamin, M.A., 1999. A comprehensive model to predict simplex atomizer performance. Journal of Engineering for Gas Turbines and Power 121, 285–294.

Liggett, J.A., Liu, P.L.-F., 1983. The Boundary Integral Equation Method for Porous Media Flow. George Allen and Unwin, London.

Lundgren, T.S., Mansour, N.N., 1988. Oscillations of drops in zero gravity with weak viscous effects. Journal of Fluid Mechanics 194, 479–510.

Park, K.S., 2008. Modeling Dense Sprays Produced by Pressure-Swirl Atomizer. M.S. Thesis, Purdue University, West Lafayette, IN.

Park, H., Heister, S.D., 2006. Nonlinear simulation of free surfaces and atomization in pressure swirl atomizer. Physics of Fluids 18, 052103.

Park, H., Yoon, S.S., Heister, S.D., 2006. On the nonlinear stability of a swirling liquid jet. International Journal of Multiphase Flow 32, 1100–1109.

Ponstein, J., 1959. Instability of rotating cylindrical jets. Applied Scientific Research 8, 425–456.

Rizk, N.K., Lefebvre, A.H., 1985. Internal flow characteristics of simplex swirl atomizer. Journal of Propulsion and Power 1, 193–199.

Rump, K., Heister, S.D., 1998. Modeling the effect of unsteady chamber conditions on atomization processes. Journal of Propulsion and Power 14, 576–579.

Sellens, R.W., 1987. Drop Size and Velocity Distributions in Sprays. A New Approach Based on the Maximum Entropy Formalism. Ph.D. Thesis, University of Waterloo, Ontario.

Sellens, R.W., 1989. Prediction of the drop size and velocity distribution in a spray, based on the maximum entropy formalism. Particle & Particle Systems Characterization 6, 17–27.

Suyari, M., Lefebvre, A.H., 1986. Film thickness measurements in simplex swirl atomizer. Journal of Propulsion and Power 2, 528–533.

Tecplot 360. 2006. User's Manual. Tecplot, Inc.

Van Der Geld, C.W.M., Vermeer, H., 1994. Prediction of drop size distributions in sprays using the maximum entropy formalism: the effect of satellite formation. International Journal of Multiphase Flow 20, 363–381.

Yoon, S.S., Heister, S.D., 2004. A nonlinear atomization model based on a boundary layer instability mechanism. Physics of Fluids 16, 47–61.

Yule, A.J., Chinn, J.J., 1994. Swirl Atomizer Flow: Classical Inviscid Theory Revisited. In: Proceedings of 6th International Conference on Liquid Atomization and Spray Systems, Rouen, France, pp. 334–341.